The Astrophysical Journal Letters, 912:L10 (8pp), 2021 May 1 https://doi.org/10.3847/2041-8213/abf502

Mapping the Universe Expansion: Enabling Percent-level Measurements of the Hubble Constant with a Single Binary Neutron-star Merger Detection

Juan Calderón Bustillo[1,2,3,4], Samson H. W. Leong[2], Tim Dietrich[5,6], and Paul D. Lasky[3,4]
[1] Instituto Galego de Física de Altas Enerxías, Universidade de Santiago de Compostela, E-15782 Santiago de Compostela, Galicia, Spain; juan.calderon.bustillo@gmail.com
[2] Department of Physics, The Chinese University of Hong Kong, Shatin, N.T., Hong Kong
[3] Monash Centre for Astrophysics, School of Physics and Astronomy, Monash University, VIC 3800, Australia
[4] OzGrav: The ARC Centre of Excellence for Gravitational-Wave Discovery, Clayton, VIC 3800, Australia
[5] Institut für Physik und Astronomie, Universität Potsdam, Karl-Liebknecht-Str. 24/25, D-14776 Potsdam, Germany
[6] Max-Planck-Institute for Gravitational Physics (Albert-Einstein-Institute), Am Mühlenberg 1, D-14476 Potsdam-Golm, Germany; samson32081@gmail.com
Received 2021 February 12; revised 2021 March 31; accepted 2021 April 6; published 2021 April 30

Abstract

The joint observation of the gravitational-wave (GW) and electromagnetic (EM) signal from the binary neutron-star merger GW170817 allowed for a new independent measurement of the Hubble constant H_0, albeit with an uncertainty of about 15% at 1σ. Observations of similar sources with a network of future detectors will allow for more precise measurements of H_0. These, however, are currently largely limited by the intrinsic degeneracy between the luminosity distance and the inclination of the source in the GW signal. We show that the higher-order modes in gravitational waves can be used to break this degeneracy in astrophysical parameter estimation in both the inspiral and post-merger phases of a neutron star merger. We show that for systems at distances similar to GW170817, this method enables percent-level measurements of H_0 with a single detection. This would permit the study of time variations and spatial anisotropies of H_0 with unprecedented precision. We investigate how different network configurations affect measurements of H_0, and discuss the implications in terms of science drivers for the proposed 2.5- and third-generation GW detectors. Finally, we show that the precision of H_0 measured with these future observatories will be solely limited by redshift measurements of EM counterparts.

Unified Astronomy Thesaurus concepts: Gravitational waves (678)

1. Introduction

The joint detection of gravitational-wave (GW) and electromagnetic (EM) radiation from the binary neutron star (BNS) merger GW170817 is a milestone for astrophysics (Abbott et al. 2017a, 2017b) that has already driven major leaps forward in a number of research areas. Among the many profound science outcomes, GW170817 provided a new, distance-ladder independent measure of the expansion of the universe (Abbott et al. 2017c; Coughlin et al. 2019; Dietrich et al. 2020), parameterized by the Hubble constant. The number of confirmed and putative BNS candidates in the third observing run (Abbott et al. 2020a) of Advanced LIGO (Aasi et al. 2015) and Advanced Virgo (Acernese et al. 2015), and the planned sensitivity increase of current- and future-generation GW detectors (Punturo et al. 2010a; Castelvecchi 2019; Reitze et al. 2019), indicates that we can expect a significant increase in both the number of detected BNS mergers, as well as signal-to-noise ratios (S/Ns) of detected events. Improvements in the high-frequency regime ($\gtrsim 1$ kHz) will also lead to the first detection of the post-merger phase of BNS mergers (Martynov et al. 2019; Ackley et al. 2020), a stage when matter effects play a significant role and most extreme densities are probed.

Determining the Hubble constant from joint GW-EM observations of BNS mergers relies on measuring the luminosity distance to the source from the GW signal and the redshift of the host galaxy from the EM counterpart (Schutz 1986; although see Messenger & Read 2012; Taylor & Gair 2012 for other methods). A key limitation of the former, however, is the degeneracy between the effects on the GW signal produced by luminosity distance and the inclination of the binary. Here, we study how this degeneracy can be broken in the context of future GW detectors in two ways: (i) via the inclusion of higher-order modes (HMs) in GW parameter estimation, and (ii) by accessing the ratio of the two GW polarisations, known as plus "+" and cross "×", using multiple detectors. For face-on binaries, we show that the inclusion of HMs leads to major improvements of the distance and inclination estimates, independently of the detector network configuration. For edge-on binaries, we find that a three-detector network that can constrain the polarization ratio and sky-location of the binary is key to correctly estimating the distance, regardless of the usage or omission of HMs. In both cases, the H_0 measurement will not be limited by our ability to infer the luminosity distance via GWs, but by the accuracy of the redshift measurement. With redshift-measurement improvements, 2% level measurements of H_0 could be possible with the observation of a single BNS located at $\sim$40 Mpc, consistent with the distance of GW170817. We show that for unequal mass systems, these improvements can be achieved with the signal emitted during the inspiral phase alone, independent of whether or not there is matter in the system; i.e., the method works for binary systems containing neutron stars and/or black holes. For equal-mass systems, we show that inclusion of matter effects in the post-merger phase is key to improving distance estimates.

We note that percent-level measurements of H_0 could be performed in a five year time-frame making use of five second-generation detectors (Chen et al. 2018), namely the two Advanced LIGO detectors (Aasi et al. 2015), Advanced Virgo (Acernese et al. 2015), KAGRA (Aso et al. 2013), and the forthcoming LIGO India (Iyer et al. 2011). However, this relies

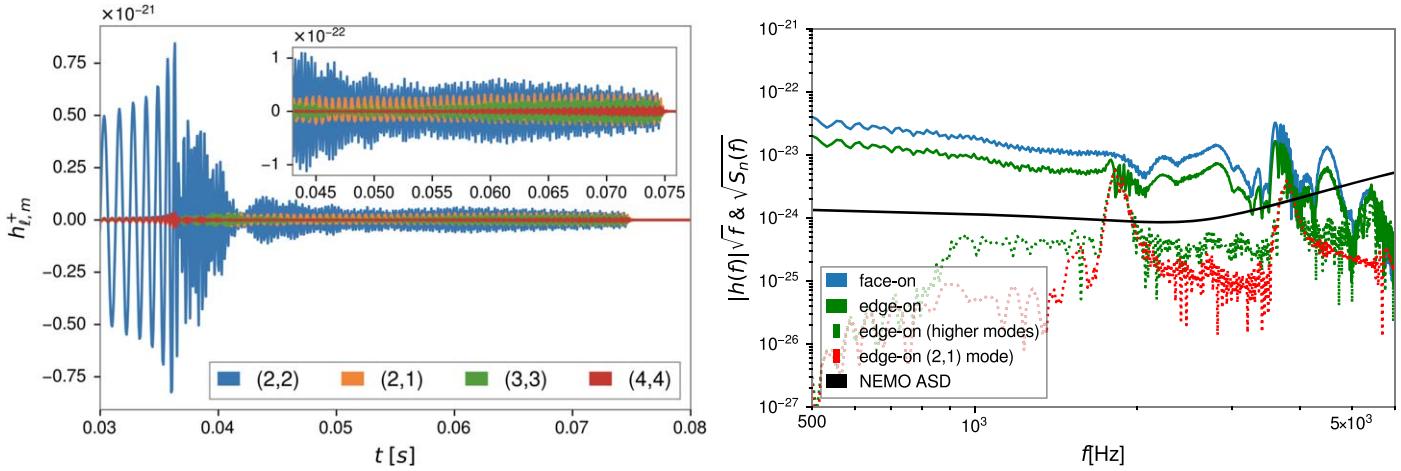

Figure 1. GW modes and full spectrum of a binary neutron star merger and its post-merger remnant for the equal-mass SLy system used in this Letter. The left panel shows the individual GW modes. The right panel shows the full spectrum of a signal observed face-on in blue, so that mainly the $(\ell, m) = (2, 2)$ mode is present, and a signal observed edge-on in green. In addition, we show the contributions from the higher-modes and the $(\ell, m) = (2, 1)$ mode. The black curve denotes the expected NEMO amplitude spectral density.

on the combination of many observations, therefore assuming that H_0 is the same in all directions and distances; i.e., the universe is statistically isotropic and homogeneous on the scales of interest. Our results help to improve this strategy as we point out that percent-level measurements with a single observation are possible. Therefore, our method paves a way toward the study of anisotropies (Collins et al. 1986) or time variations of H_0 (Wu et al. 1996), to obtain a significantly better and more detailed understanding of the evolution history of our universe.

1.1. Higher-order Modes of Compact Binary Mergers

The "+" and "×" polarizations of a GW emitted by a compact binary merger located at a luminosity distance d_L can be expressed as a superposition of individual modes, $h_{\ell,m}$, weighted by spin -2 spherical harmonics $Y^{-2}_{\ell,m}$ as

$$h_+ - ih_\times = \frac{1}{d_L}\sum_{\ell\geqslant 2}\sum_{m=-\ell}^{m=\ell} Y^{-2}_{\ell,m}(\iota, \varphi)h_{\ell,m}(\Xi). \quad (1)$$

Here, Ξ denotes the masses m_i and dimensionless spins $\boldsymbol{\chi}_i$ of the individual objects and, for the case of BNSs, the individual tidal deformabilities Λ_i characterizing the deformation of each star in the external gravitational field of the companion. The parameters (ι, φ) represent the polar and azimuthal angles of a spherical coordinate frame describing the location of the observer around the binary (or conversely, the orientation of the binary with respect to the observer), with $\iota = 0$ denoting the direction of the orbital angular momentum of the binary and $\iota = \pi/2$ denoting the orbital plane. These values, respectively, refer to face-on and edge-on oriented binaries. For nonprecessing binaries, the above sum is dominated by the quadrupole $(\ell, m) = (2, \pm 2)$ modes while HMs become loud only during the final inspiral and merger phase, with increasing relative amplitude as the mass ratio $q = m_1/m_2 \geqslant 1$ increases (Pekowsky et al. 2013; Varma et al. 2014; Bustillo et al. 2015; Calderón Bustillo et al. 2017).

Current parameter estimation of BNS signals makes use of waveform templates including only the quadrupole mode. This causes a degeneracy between the inclination and distance parameters that fundamentally limits our ability to measure each. Several works have shown that inclusion of HMs in templates can break this degeneracy for sources with sufficiently loud HMs in the detector sensitive band, as the observed combination of modes will depend on the orientation of the binary via the $Y_{\ell,m}$ factors (Graff et al. 2015; Calderón Bustillo et al. 2018; London et al. 2018; Pang et al. 2018; Calderón Bustillo et al. 2019). For Advanced LIGO and Virgo observations, unfortunately, this is only possible for large mass and asymmetric BBHs (Graff et al. 2015; London et al. 2018; Chatziioannou et al. 2019; LIGO Scientific Collaboration 2020) for which the merger and ringdown emission, rich in HMs, is strong in the detector sensitive band. In contrast, the merger and post-merger of BNSs is unobservable due to its large frequency. This emission will, however, be observable with future high-frequency (Martynov et al. 2019; Ackley et al. 2020) and third-generation (Punturo et al. 2010a; Reitze et al. 2019) detectors and, in addition, the pre-merger GW emission will last for several minutes in the sensitive detector band, allowing us to accumulate the effect of weak HMs.

2. Analysis Setup

2.1. Binary Neutron-star Waveforms

We test our ability to measure the source distance and H_0 using the inspiral and post-merger emission of BNSs. To this, we perform parameter inference on two kinds of simulated GW signals. First, we use 80 ms long numerical-relativity simulations for the post-merger emission of BNS (Dietrich & Hinderer 2017). These have mass ratios $q = 1$ and $q = 1.5$ and implement two different equations of state (EOSs): a soft one (SLy) and a stiff one (MS1b [7]). The left panel of Figure 1 shows the time domain modes for the equal-mass SLy case located at a distance of 40 Mpc. The right panel shows in blue and green the spectra of full waveforms observed face-on (blue) and edge-on (green), together with the contribution of the HMs and the $(\ell, m) = (2, 1)$ mode alone for the edge-on

[7] While a stiff EOS like MS1b is disfavored by the observation of GW170817 and its EM counterparts (e.g., Abbott et al. 2019, 2018; Dietrich et al. 2020), it provides a good test case for our study to show the effect of two different EOSs.

case. It can be noted not only how the face-on signal is stronger, but how the presence of HMs in the edge-on signal leads to noticeable morphological differences. Parameter inference on these short waveforms provides an idea of how the post-merger emission breaks the distance-inclination degeneracy. Restricting to this and ignoring the long inspiral signal, however, would greatly underestimate the S/N accumulated throughout the full minutes-long signal observable by the detector, reducing the accuracy of our measurements.

To obtain signals that can cover the full inspiral and post-merger emission from a BNS, we combine (Bustillo et al. 2015) our short numerical-relativity waveforms (Dietrich & Hinderer 2017) with long analytical waveforms covering the early inspiral minutes before the merger (e.g., computed using the tidal effective-one-body model of Nagar et al. 2018). Unfortunately, parameter inference using these waveforms is computationally prohibitive. As a solution, we implement a two-step approach. First, we consider 128 s long phenomenological (phenom) waveforms (Khan et al. 2016; Santamaria et al. 2010), constructed with the `IMRPhenomHM` model (London et al. 2018), covering the inspiral-merger and ringdown stages of nonprecessing binary black hole (BBH) mergers. While computationally inexpensive, these waveforms omit the two main characteristic aspects of BNSs: tidal-deformability effects and the post-merger emission shown in Figure 1. Since, as argued, the latter can improve our distance measurements, results obtained using this BBH signal model are rather conservative. Finally, in order to obtain improved and more realistic results for BNSs, we combine these BBH parameter estimates with those obtained by solely analyzing the short numerical-relativity waveforms covering the post-merger stage of BNSs, following the procedure described in Zimmerman et al. (2019).

2.2. Analysis Setup

We inject signals $h(\theta_{\rm true})$ with source parameters $\theta_{\rm true}$, that include HMs, in zero noise and estimate the source parameters using waveform templates $h(\theta)$ that omit and include HMs. We compute the posterior Bayesian probability of the parameters θ as

$$p(\theta|\theta_{\rm true}) = \frac{\pi(\theta)\mathcal{L}(\theta|h(\theta_{\rm true}))}{\int \pi(\theta)\mathcal{L}(\theta|h(\theta_{\rm true}))d\theta}, \quad (2)$$

with $\pi(\theta)$ denoting the prior probability of the parameters θ and $\mathcal{L}(\theta|h(\theta_{\rm true}))$ denoting their likelihood. As usual, the latter is defined as the standard frequency-domain likelihood for GW transients (Finn 1992; Romano & Cornish 2017)

$$\log \mathcal{L}(\theta|h(\theta_{\rm true})) \propto -\sum_N \frac{(h(\theta_{\rm true}) - h(\theta)|h(\theta_{\rm true}) - h(\theta))}{2}, \quad (3)$$

where N runs over the different detectors of our network. As we discuss later, we work with two- and three-detector networks. As usual, $(a|b)$ represents the inner product (Cutler & Flanagan 1994)

$$(a|b) = 4\Re \int_{f_{\rm min}}^{f_{\rm max}} \frac{\tilde{a}(f)\tilde{b}^*(f)}{S_n(f)} df, \quad (4)$$

where $\tilde{a}(f)$ denotes the Fourier transform of $a(t)$ and * denotes the complex conjugate. The factor $S_n(f)$ denotes the one-sided power spectral density of the detector. In this work, we consider a network of detectors, all with noise sensitivity equivalent to that of the proposed 2.5-generation Neutron star Extreme Matter Observatory (NEMO; Ackley et al. 2020). We choose a lower frequency cutoff of $f_{\rm min}=20$ Hz and a sampling frequency of 16 kHz so that $f_{\rm max}=8$ kHz. The NEMO detector has a proposed sensitivity similar to the Cosmic Explorer and Einstein Telescope in the kilohertz regime; we could equally use those third-generation detectors and achieve similar results for the late inspiral and post-merger, albeit with larger signal-to-noise ratios for the full signal given the better low-frequency ($\lesssim$500 Hz) sensitivity.

In all cases, we assume standard prior probabilities for the sky-location, source orientation, and polarization angle, together with a prior uniform in comoving volume and a uniform prior on the time-of-arrival, with a width of 0.2 s, centered on the true value. For our analyses making use of 128 s long phenom waveforms, we impose uniform priors on the individual masses $m_{1,2} \in [1, 2]\, M_\odot$ and on the components of the individual spins along the orbital angular momentum $\chi^z_{1,2} \in [-0.15, 0.15]$. Since numerical-relativity waveforms, however, are only produced for a discrete set of intrinsic parameters, we assume the masses and spins to be known in this case. We find this is a reasonable assumption as the individual masses and the effective spin parameter (Santamaria et al. 2010) $\chi_{\rm eff} = (\chi^z_1 m_1 + \chi^z_2 m_2)/(m_1 + m_2)$ are very well measured from the long inspiral. As an example, with a triple-detector network and using HMs, we determine the total mass, chirp mass, and effective-spin parameters of our face-on unequal-mass source with respective uncertainties of $<1\%$, $<0.01\%$, and <0.015 at the 68% level. We perform our parameter inference runs with the software `Bilby` (Ashton et al. 2019; Smith et al. 2020), sampling the parameter with the algorithm `CPNest` (Veitch et al. 2020).

We consider three network configurations. The first (denoted HV) assumes two detectors with the location and orientation of Advanced LIGO Hanford and Virgo. Such a network has each detector sensitive to one of the two independent GW polarizations. The second network (HL) assumes LIGO Hanford and Livingston location and orientations, almost anti-aligned, so that both detectors are sensitive to roughly the same GW polarization, missing the other one. Finally, we consider an HLV network that is sensitive to both GW polarizations and can pinpoint the sky-location of the source.

The accuracy of our distance measurement is of course limited by the loudness of the injected signals in our detector network, quantified by the optimal network S/N, given by

$$\rho_{\rm opt}(h(\theta_{\rm true})) = \sqrt{\sum_N (h(\theta_{\rm true})|(h(\theta_{\rm true}))_N}, \quad (5)$$

which is inversely proportional to the source luminosity distance d_L. As we show in Appendix C, for face-on cases we obtain optimal S/Ns of $\sim$190 for HL and HLV networks and $\sim$140 for HV. In contrast, for the weaker edge-on cases we obtain respective values $\rho_{\rm opt} \in [30, 65]$ depending on the mass ratio and network considered. For comparison, the S/N of GW170817, whose source was rather face-on, was only $\simeq 32$. We note that while in this study we restrict to sources placed at distances $d_{L,\rm true} = 40$ Mpc, our results can be extended to different reference distances. In particular, in our S/N-regime,

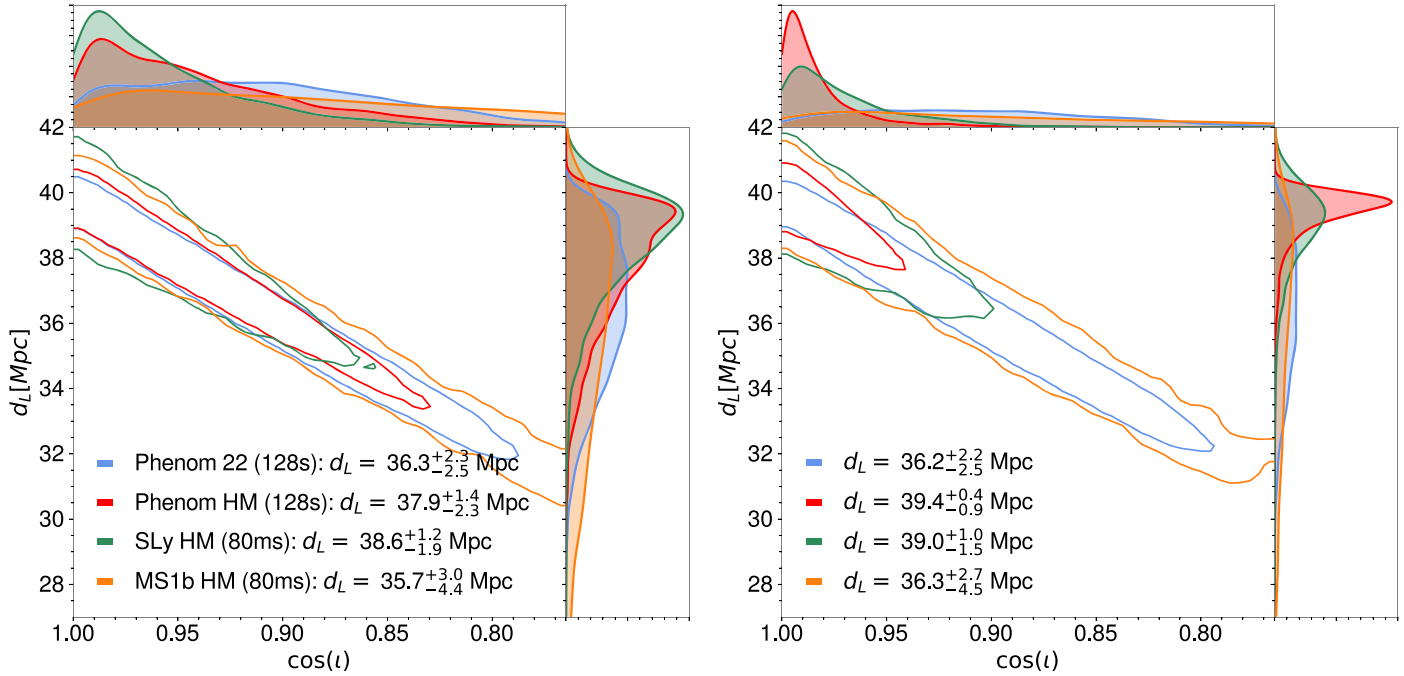

Figure 2. Two-dimensional posterior distributions for the luminosity distance and inclination angle of a face-on ($\cos(\iota) = 1$) binary neutron star merger located at 40 Mpc, with mass ratio $q = 1$ (left) and $q = 1.5$ (right) and a total mass of $M = 2.75\ M_\odot$. The contours delimit the 90% credible regions obtained by analyzing a 128 s waveform including (red) and omitting (blue) higher-order modes. Also shown are posterior reconstructions using waveforms that only cover the last 80 ms of the merger and ringdown modeled with numerical relativity simulations with two different EOSs (orange and green). The labels quote median values and symmetric 68% credible intervals for the luminosity distance.

given fixed source and detector network, the uncertainty of our distance estimates roughly depends on the optimal S/N (and therefore on the reference distance) as $\Delta(d_L) \propto 1/\rho^2_{\rm opt} \propto d^2_{L,\rm true}$ (Rao 1992; Cramer 1999; Li 2013). In addition, uncertainties in the estimated value of the Hubble constant $H_0 = cz/d_{L,\rm true}$ grow linearly with distance.

2.3. Target Binary Neutron-star Sources

We choose four target sources with total mass $M = 2.75\ M_\odot$, mass ratios $q = 1$ and $q = 1.5$, and oriented both face-on ($\iota = 0$) and edge-on ($\iota = \pi/2$). Signals emitted in these two angles differ in three aspects: morphology, polarization, and loudness. Face-on signals contain solely the $(\ell,\ m) = (2,\ 2)$ mode, are circularly polarized (i.e., both $h_{+,\times}$ have the same amplitude), and are louder than edge-on signals. On the contrary, edge-on signals have contributions from higher-order emission modes that confer a richer structure, but are weaker in amplitude than face-on ones (see Figure 1). In addition, edge-on signals contain only one of the two polarizations. Consequently, it has been shown that measuring the ratio of the two polarizations is key to correctly inferring the inclination of the source, provided that the detector network can observe both polarizations (Usman et al. 2019). For each of these sources, we consider two EOSs, namely `SLy` and `MS1b`, which we assume to be known. Different EOSs trigger post-merger HMs in different ways, varying the accuracy of the distance estimate. Finally, we would ideally consider a wide range of distances and sky locations for all of our target sources. However, given the extreme computational cost of our parameter inference runs, and to allow for a direct comparison of our results, we place all of our sources at the same distance and sky location. For the former, we considered that the most reasonable choice was a value of $d_L = 40$ Mpc, consistent with that of GW170817, the only conclusive BNS observed to date through GWs. Finally, we placed all of our target sources at the same, arbitrary sky location.

3. Results

3.1. Distance Estimates

Figure 2 shows the two-dimensional posterior distributions for the luminosity distance and inclination of face-on oriented binaries with mass ratios of $q = 1$ (left) and $q = 1.5$ (right), using an HLV detector configuration. The contours denote the 90% credible regions and the legend provides median estimates with symmetric 68% credible intervals. For unequal masses, and using 128 s long phenom waveforms, the omission of HMs in the templates $h(\theta)$ leads to a biased estimate of $d_L^{\rm Phenom,\ 22} = 36.2^{+2.2}_{-2.5}$ Mpc. Their inclusion corrects this bias and reduces the uncertainty by $\sim$70%, yielding a distance measurement of $d_L^{\rm Phenom,\ HM} = 39.4^{+0.4}_{-0.9}$. For equal masses, the impact of HMs is significantly milder, as the (usually strongest) odd-m emission modes are suppressed (Pan et al. 2011, 2014; Blanchet 2014). This leads to a biased estimate of $d_L^{\rm Phenom,\ HM} = 37.9^{+1.4}_{-2.3}$ even if HMs are included. We also note that this remains true even if one would assume the intrinsic source parameters (masses and spins) to be known. This situation changes, however, when using 80 ms long numerical-relativity waveforms that can account for the rich post-merger signal morphology. For both mass ratios, and considering a `SLy` equation of state, results are better than those making use of 128 s long phenom waveforms omitting HMs. Moreover, for equal-mass, the estimate even improves on that including HMs, yielding a nonbiased estimate $d_L^{\rm SLy} = 38.6^{+1.8}_{-2.7}$ with smaller uncertainties.

We combine the distance estimates obtained using numerical-relativity waveforms with those obtained analyzing phenom waveforms restricted to frequencies not covered by the former. To this, we multiply the respective posterior distributions for the distance, dividing by one instance of the prior (Zimmerman et al. 2019).[8] We obtain joint estimates of $d_L^{\rm joint} = 38.6^{+0.9}_{-1.3}$ Mpc for the $q = 1$ case and $d_L^{\rm joint} = 39.4^{+0.4}_{-0.7}$ for the $q = 1.5$ case. The reason behind this improvement is that matter effects arising during the post-merger of BNSs trigger HMs, helping to break the degeneracy between distance and inclination and even allowing us to measure the azimuthal angle (see Appendix B). For the unequal-mass case, these only add a small contribution with respect to the integrated effect of the HMs during the 128 s of signal. For $q = 1$, however, odd-m modes are suppressed during the inspiral and are only triggered during the post-merger of our numerical-relativity simulations due to an effect known as one-armed spiral instability or 21-mode instability (East et al. 2016; Lehner et al. 2016; Radice et al. 2016; see Appendix B). As a consequence, the inclusion of the post-merger emission can have a large impact. In our study, the distance estimates are much better for SLy compared to MS1b, due to the stronger HM emission.

Finally, while we have discussed results assuming an HLV detector network, in the Suppl. Material we show results for all studied network configurations. In all cases we obtain similar results, both qualitatively and quantitatively.

3.2. Edge-on Cases

Previous work has shown that the degeneracy between distance and inclination can be broken by computing the ratio $h_\times/h_+$, as this evolves from 1 to 0 as the inclination varies from face-on to edge-on (Usman et al. 2019). We find that for face-on binaries, all HL, HV, and HLV configurations yield almost equivalent distance measurements despite the differences in signal loudness across the network, so that HMs have a much larger impact on the measurement than the polarization ratio. In contrast, in Figure 3 we show that for edge-on cases it is key not only to access both signal polarisations but also to have a third detector that can pin-point the sky-location of the source. For an HLV configuration, unbiased estimates with uncertainties lower than 4% are obtained regardless of the usage of HMs, while biased estimates are obtained using both two-detector configurations. The reason is that such configurations cannot pin-point the sky location of the source using timing information. This way, Bayesian inference places the source at those patches of the sky, consistent with the two-detector timing, where the detector network is most sensitive, biasing the distance toward large values. We obtain identical qualitative results for the $q = 1$ case, as well as when analyzing our 80 ms long numerical-relativity simulations.

3.3. Hubble Constant Estimates

Combining our distance estimates with simulated redshift estimates, we can infer H_0 via $H_0 = cz/d_L$, with c being the speed of light. We assume redshift estimates consisting of Gaussian posterior distributions centered at a value of $z_0 = 0.00897$, corresponding to $d_L = 40$ Mpc in a ΛCDM cosmology with Hubble parameter $H_0 = 67.9$ km s^{-1} Mpc^{-1}. We assume that the redshift has an uncertainty with standard deviation Δz ranging from a realistic value of 10^{-3} consistent with that for GW170817 (Abbott et al. 2017c) to an improved value of 10^{-4} which would require higher resolution spectrograms and also the possibility to measure the internal motion of sources within individual galaxies, e.g., (Davis et al. 2019).

Figure 4 shows the H_0 estimates derived from the distance measurements of our face-on BNSs with mass ratios $q = 1$ and $q = 1.5$ as a function of Δz using an HLV network. Once again, we quote results in terms of symmetric 68% credible intervals centered at the median value. For unequal mass, and for $\Delta z = 10^{-3}$, the omission of HMs never leads to biased estimates. Their inclusion, however, leads to an important improvement from $H_0 = 73.8^{+9.0}_{-9.8}$ to $H_0 = 68.3^{+7.5}_{-7.5}$. More spectacularly, for the most optimistic $\Delta z = 10^{-4}$ HMs improve the measurement from $H_0 = 73.8^{+5.3}_{-4.1}$ to $H_0 = 68.0^{+1.6}_{-1.0}$, enabling a 2%-level measurement. This shows that with 2.5 G detectors, together with improved detector calibration and waveform models, H_0 estimates will be limited by EM redshift measurements and not by GW distance ones. Conversely, if HMs are omitted, a significant reduction of Δz will not translate into an improved H_0 estimate. Moreover, we find that H_0 estimates would be biased when $\Delta z \lesssim 0.5$. Consistently with the previous section, the inclusion of the post-merger emission in the analysis does not lead to any relevant improvement.

As expected, the situation is different for equal-mass cases. For these, the inclusion of post-merger effects is crucial to obtain visible improvements in the H_0 measurement. For $\Delta z = 10^{-3}$ we obtain a mild improvement from $H_0 = 71.2^{+8.6}_{-8.3}$ to $H_0 = 69.6^{+7.8}_{-7.7}$. When Δz is reduced to $\Delta z = 10^{-4}$, the HMs present in the post-merger emission allow for an estimate $H_0 = 69.3^{+2.5}_{-1.5}$, with uncertainties at the $\simeq$4% percent level, while their omission doubles the uncertainty and biases the measurement.

Almost identical results hold for the HL and HV networks, as shown in the Suppl. Material. For the (weaker) edge-on binaries, we find percent-level measurements are possible using the HLV network regardless of the usage of HMs.

4. Conclusions

We have shown that the use of HMs in parameter inference of compact binaries with masses in the BNS range leads to great improvements of the distance and inclination estimates in the context of future detectors sensitive to signals in the ∼kilohertz regime, such as the proposed 2.5-generation instruments presented in Martynov et al. (2019) and Ackley et al. (2020) and full third-generation interferometers (Punturo et al. 2010a; Reitze et al. 2019). For face-on binaries with modest mass ratios of $q = 1.5$, we find that the accumulated effect of the HMs during the inspiral reduces the uncertainties by ≈70%. At the current state-of-the-art of redshift measurements from EM counterparts, this yields an ≈25% improvement of H_0 estimates. With improved redshift estimates, HMs can enable measurements of H_0 near the subpercent level with a single observation. For equal-mass binaries, the HMs emitted during the post-merger stage are crucial to improve H_0 estimates. A soft EOS like SLy, favored by current observations, would enable percent-level measurements. For edge-on cases, we find that it is crucial to have a three-detector, HLV-like network, able to constrain the inclination and the sky-location of the binary.

[8] Note that this ignores that stronger constraints can be obtained for the inclination and the sky-location by combining both measurements, making our results rather conservative.

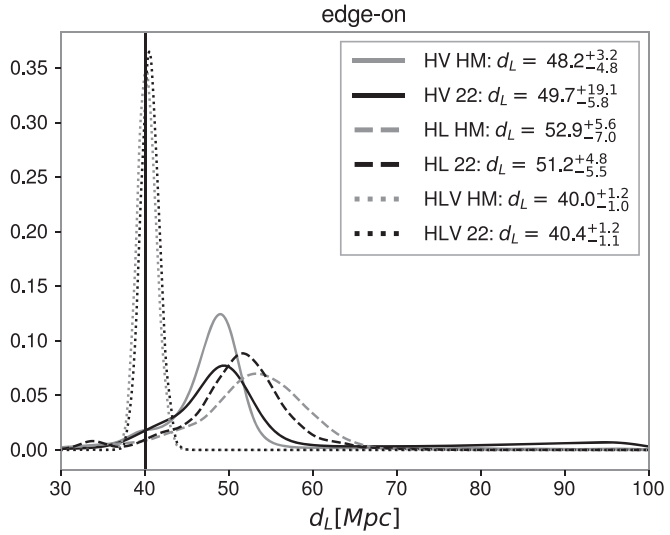

Figure 3. Luminosity distance estimates for a binary neutron star merger with mass ratio $q = 1.5$ and total mass $M = 2.75\,M_\odot$ located at 40 Mpc using different detector configurations and omitting/including higher-order modes in the analysis of the signal. We quote median values and symmetric 68% credible intervals. The injected signals are 128 s long IMRPhenomHM waveforms including higher-order modes.

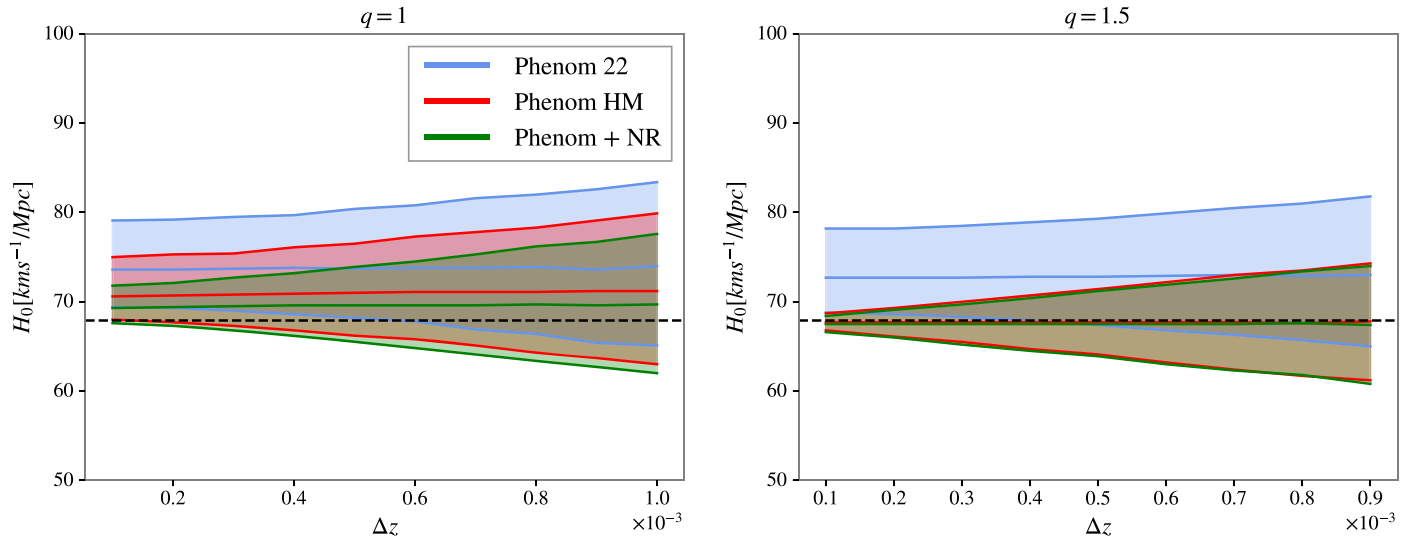

Figure 4. Estimates of H_0 derived from the distance estimates of face-on binaries with mass ratios $q = 1$ (left) and $q = 1.5$ (right) located at a distance of 40 Mpc, and assuming redshift measurement of $z = 0.00897 \pm \Delta z$. We consider a three-detector network in an HLV configuration with NEMO sensitivity curves. The contours delimit 68% credible intervals. We show results using phenom waveforms for binary black holes omitting and including HMs in blue and red, respectively. In green, we show combined results for phenom and post-merger numerical-relativity waveforms including HMs.

We have focused on single event analyses, assuming a constant value for H_0. Significantly more precise measurements of the Hubble constant will be achievable by combining this method with an ensemble of BNS detections in the not-too-distant future. The precision of the estimates we obtain with single events may enable us to study possible time variations (Wu et al. 1996) and anisotropies (Collins et al. 1986) of H_0. While we have restricted to the reasonable paradigm of a GW170817-like source located at 40 Mpc, we note that current BNS merger-rate estimates suggest that such an event is rather rare, with less than 0.1 such mergers per year (Abbott et al. 2020b). Pushing this value to at least one per year would require the consideration of sources at $\simeq$90 Mpc, halving the S/N of our signals, multiplying by four our distance uncertainties and doubling that for H_0. We note, however, that this would still allow for 4%-level measurements of H_0. Furthermore, and most importantly, we have considered the fairly conservative scenario of a network formed by 2.5-generation detectors like NEMO, which resulted in S/Ns ranging in 50–200 (see Appendix C). The replacement of two of these detectors by other projected detectors like Cosmic Explorer (Abbott et al. 2017d; Reitze et al. 2019) or Einstein Telescope (Hild et al. 2010; Punturo et al. 2010b), more sensitive at low frequencies and as sensitive at high frequencies as NEMO, does raise these S/Ns to the order of 1000, which would lead to significantly more precise results.

We thank Rory Smith, Avi Vajpeyi, and Sylvia Biscoveanu for their help setting up `Parallel Bilby` (Smith et al. 2020) runs. We thank Nicolas Sanchis-Gual, Ornella Piccinni, Valentin Christiaens, and Ricardo Martinez-Garcia for comments on the manuscript and Tjonnie Li for useful discussions. J.C.B. acknowledges support by the Australian Research Council (ARC) Discovery Project DP180103155 and the Direct Grant, Project 4053406, from the Research Committee of the Chinese University of Hong Kong. The project that gave rise to these results also received the support of a fellowship from the "la Caixa" Foundation (ID 100010434) and from the European Union's Horizon 2020 research and innovation program under the Marie Skłodowska-Curie grant agreement No. 847648. The fellowship code is LCF/BQ/PI20/11760016. P.D.L. is supported through ARC Future Fellowship FT160100112, ARC Discovery Project DP180103155, and ARC Centre of Excellence CE170100004. The authors acknowledge computational resources provided by the LIGO Laboratory and supported by National Science Foundation Grants PHY-0757058 and PHY0823459; and the support of the NSF CIT cluster for the provision of computational resources for our parameter inference runs, and the support of the CUHK Central High Performance Computing Cluster, on which our runs using Parallel Bilby were performed. Part of the work described in this paper was supported by a grant from the Croucher Foundation of Hong Kong. This document has LIGO DCC number LIGO-P2000160.

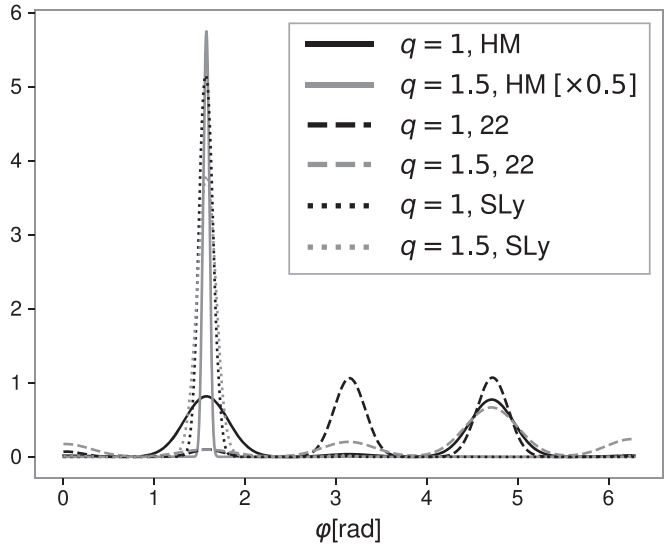

Figure 5. Estimation of the azimuthal angle for two edge-on compact binaries with mass ratios $q = 1$ (black) and $q = 1.5$ (gray). The solid and dashed lines denote estimates making use of 128 s long phenom models for BBHs, respectively, including and omitting HMs. The dotted lines denote estimates based on 80 ms long BNS simulations including HMs. For $q = 1$, only the usage of numerical-relativity waveforms allows for an unambiguous estimation of the azimuth.

Appendix A
Measuring the Azimuthal Angle

The inclusion of HMs in the templates accounts for asymmetries in the GW emission that cannot be reproduced when HMs are omitted. This asymmetry allows us to define preferred directions in the orbital plane to determine in an unambiguous way where the observer is sitting on it, providing a clear physical meaning to the azimuth angle φ (Calderón Bustillo et al. 2019). For instance, for the case of BBHs, this was used to determine the direction of the final recoil velocity with respect to the line of sight (Calderón Bustillo et al. 2018). While this would lead to accurate measurements of the kick introduced by GW radiation (Calderón Bustillo et al. 2018), it might not account for the final velocity of the remnant due to the ejection of material during the merger process, (e.g., Kyutoku et al. 2015; Chaurasia et al. 2020). Figure 5 shows the posterior distributions for the φ for two edge-on binaries with mass ratios $q = 1$ and $q = 1.5$, using an "HLV" network. Results are shown for 128 s long phenom waveforms including and omitting HMs, and for 80 ms long numerical-relativity waveforms implementing a SLy EOS and including HMs. For unequal masses, HMs allow for an extremely accurate estimate without the need to include post-merger effects. For equal-mass systems, however, this kind of measurement is only possible once the post-merger is included. In concordance with the results shown in Figures 2 and 4, the measurement is less precise for MS1b, due to its weaker HMs.

Appendix B
Exploiting the One-armed Inspiral Instability

For the case of BBHs, HMs have very little contribution to the GW emission when the mass ratio is close to one. Thus, the large effect of the HMs for the measurement of the Hubble constant might seem somewhat unexpected. Moreover, Figure 1 shows that the contribution from the HMs in the postmerger phase is dominated by that of the (2, 1) mode, which is particularly surprising for the case of the equal-mass binary, for which odd-m modes are completely suppressed for black hole binaries by the symmetry of the problem. Past work has shown that tiny asymmetries in the binary configuration can develop into a large asymmetry in the merger stage known as one-armed spiral instability, triggering a strong (2, 1) mode, (e.g., Lehner et al. 2016; East et al. 2016; Radice et al. 2016). Figure 1 shows that this leads to "kinks" in the GW spectrum at a frequency of approximately half of the main emission peak. This feature grows as the binary is observed edge-on and its exact morphology depends strongly on the azimuthal angle. The importance of the (2, 1) mode suggests that we are in fact exploiting the one-armed spiral instability to infer the orientation of the binary. To check this, we repeated our analyses using numerical-relativity waveforms including only the $(\ell, m) = (2, 2)$ and (2, 1) modes obtaining results quantitatively identical to those including the rest of the modes.

Appendix C
Tables of Estimates for Face-on Binaries

In Tables 1 and 2 we report all luminosity distances and H_0 estimates obtained for face-on cases using phenom waveforms including and omitting HMs, and combining phenom and numerical-relativity estimates assuming a SLy EOS. In order to provide an idea of the loudness of these injections, we quote optimal S/Ns for those performed using the PhenomHM model, adding those for the edge-on cases within parentheses. For comparison, note that the S/N of GW170817, rather face-on, was of only $\simeq$32, much lower than that of our weak edge-on injections. As throughout the main body of the paper, we quote median values and symmetric 68% credible intervals. For our edge-on binaries, as shown in Figure 3, two detector networks produce extremely biased results and measurements are independent of the usage of HMs.

Table 1
Luminosity Distance and H_0 Estimates for a face-on Binary with Mass Ratio $q = 1$ and Total Mass $M = 2.75\,M_\odot$ Located at a True Distance of 40 Mpc Using Different Waveform Models and Detector Network Configurations

Waveform Model	d_L [Mpc]			H_0 [km s^{-1}/Mpc] ($\Delta z = 10^{-3}$)			H_0 [km s^{-1}/Mpc] ($\Delta z = 10^{-4}$)		
	HLV	HV	HL	HLV	HV	HL	HLV	HV	HL
Optimal S/N	198.67 (63.58)	141.18 (52.97)	189.17 (56.96)						
Phenom (2, 2)	$36.3^{+2.3}_{-2.5}$	$35.7^{+2.4}_{-3.7}$	$32.8^{+5.0}_{-6.5}$	$73.9^{+9.6}_{-8.8}$	$74.3^{+10.4}_{-9.3}$	$81.8^{+18.9}_{-13.1}$	$73.6^{+5.4}_{-4.2}$	$72.8^{+7.3}_{-4.8}$	$81.2^{+18.4}_{-10.2}$
Phenom HM	$37.9^{+1.4}_{-2.3}$	$38.1^{+1.4}_{-2.8}$	$37.5^{+1.8}_{-3.1}$	$71.2^{+8.8}_{-8.3}$	$73.2^{+9.5}_{-9.0}$	$72.2^{+9.0}_{-7.8}$	$70.6^{+4.4}_{-2.5}$	$72.5^{+6.1}_{-4.0}$	$71.4^{+5.9}_{-3.3}$
Phenom HM + NR[SLy]	$38.6^{+0.9}_{-1.3}$	$38.4^{+1.0}_{-1.7}$	$38.4^{+1.0}_{-2.2}$	$69.6^{+7.8}_{-7.7}$	$69.8^{+7.1}_{-7.5}$	$70.3^{+8.0}_{-7.8}$	$69.3^{+2.5}_{-1.5}$	$69.3^{+1.9}_{-2.9}$	$69.8^{+3.2}_{-2.0}$

Note. We quote median values and symmetric 68% credible intervals. In the first row, we provide the optimal network S/Ns of the injections performed with PhenomHM. For completeness, we also add within a parenthesis the value for the edge-on versions, which is significantly lower.

Table 2
Luminosity Distance and H_0 Estimates for a Face-on Binary with Mass Ratio $q = 1.5$ and Total Mass $M = 2.75\ M_\odot$ Located at a True Distance of 40 Mpc Using Different Waveform Models and Detector Network Configurations

Waveform Model	d_L [Mpc]			H_0 [km s^{-1}/Mpc] ($\Delta z = 10^{-3}$)			H_0 [km s^{-1}/Mpc] ($\Delta z = 10^{-4}$)		
	HLV	HV	HL	HLV	HV	HL	HLV	HV	HL
Optimal S/N	194.44 (62.23)	149.14 (34.40)	185.15 (55.75)						
Phenom (2, 2)	$36.2^{+2.2}_{-2.5}$	$36.0^{+2.5}_{-3.4}$	$34.2^{+3.7}_{-5.1}$	$73.8^{+9.0}_{-9.8}$	$74.8^{+12.3}_{-9.3}$	$77.0^{+11.7}_{-10.6}$	$73.8^{+5.3}_{-4.1}$	$74.2^{+7.5}_{-4.7}$	$78.1^{+13.3}_{-7.5}$
Phenom HM	$39.4^{+0.4}_{-0.9}$	$38.9^{+0.8}_{-2.1}$	$38.5^{+1.1}_{-2.3}$	$68.3^{+7.5}_{-7.5}$	$69.5^{+8.4}_{-7.8}$	$74.1^{+10.1}_{-9.2}$	$68.0^{+1.6}_{-1.1}$	$68.9^{+3.6}_{-1.7}$	$69.5^{+4.2}_{-2.1}$
Phenom HM + NR[SLy]	$39.4^{+0.4}_{-0.7}$	$38.9^{+0.8}_{-2.3}$	$39.0^{+0.7}_{-1.1}$	$68.1^{+7.2}_{-7.3}$	$69.0^{+7.8}_{-7.7}$	$67.4^{+5.8}_{-5.7}$	$68.0^{+1.2}_{-1.0}$	$68.7^{+1.9}_{-1.4}$	$68.8^{+2.3}_{-1.5}$

Note. We quote median values and symmetric 68% credible intervals. In the first row, we provide the optimal network S/Ns of the injections performed with PhenomHM. For completeness, we also add within parentheses the value for the edge-on versions, which is significantly lower.

ORCID iDs

Juan Calderón Bustillo https://orcid.org/0000-0002-4171-5884
Samson H. W. Leong https://orcid.org/0000-0003-0470-282X
Tim Dietrich https://orcid.org/0000-0003-2374-307X
Paul D. Lasky https://orcid.org/0000-0003-3763-1386

References

Aasi, J., Abbott, B. P., Abbott, R., et al. 2015, CQGra, 32, 074001
Abbott, B. P., Abbott, R., Abbott, T. D., et al. 2017a, PhRvL, 119, 161101
Abbott, B. P., Abbott, R., Abbott, T. D., et al. 2017b, ApJL, 848, L12
Abbott, B. P., Abbott, R., Abbott, T. D., et al. 2017c, Natur, 551, 85
Abbott, B. P., Abbott, R., Abbott, T. D., et al. 2017d, CQGra, 34, 044001
Abbott, B. P., Abbott, R., Abbott, T. D., et al. 2018, PhRvL, 121, 161101
Abbott, B. P., Abbott, R., Abbott, T. D., et al. 2019, PhRvX, 9, 011001
Abbott, B. P., Abbott, R., Abbott, T. D., et al. 2020a, arXiv:2001.01761
Abbott, R., Abbott, T. D., Abraham, S., et al. 2020b, Population Properties of Compact Objects from the Second LIGO-Virgo Gravitational-Wave Transient Catalog, arXiv:2010.14533
Acernese, F., Agathos, M., Agatsuma, K., et al. 2015, CQGra, 32, 024001
Ackley, K., Adya, V. B., Agrawal, P., et al. 2020, PASA, 37, e047
Ashton, G., Hübner, M., Lasky, P. D., et al. 2019, ApJS, 241, 27
Aso, Y., Michimura, Y., Somiya, K., et al. 2013, PhRvD, 88, 043007
Blanchet, L. 2014, LRR, 17, 2
Bustillo, J. C., Bohé, A., Husa, S., et al. 2015, arXiv:1501.00918
Calderón Bustillo, J., Clark, J. A., Laguna, P., & Shoemaker, D. 2018, PhRvL, 121, 191102
Calderón Bustillo, J., Evans, C., Clark, J. A., et al. 2019, arXiv:1906.01153
Calderón Bustillo, J., Laguna, P., & Shoemaker, D. 2017, PhRvD, 95, 104038
Castelvecchi, D. 2019, Natur, 566, 305
Chatziioannou, K., Cotesta, R., Ghonge, S., et al. 2019, PhRvD, 100, 104015
Chaurasia, S. V., Dietrich, T., Ujevic, M., et al. 2020, arXiv:2003.11901
Chen, H.-Y., Fishbach, M., & Holz, D. E. 2018, Natur, 562, 545
Collins, C. A., Joseph, R. D., & Robertson, N. A. 1986, Natur, 320, 506
Coughlin, M. W., Dietrich, T., Heinzel, J., et al. 2019, arXiv:1908.00889
Cramer, H. 1999, Mathematical Methods of Statistics (Princeton, NJ: Princeton Univ. Press)
Cutler, C., & Flanagan, É. E. 1994, PhRvD, 49, 2658
Davis, T. M., Hinton, S. R., Howlett, C., & Calcino, J. 2019, MNRAS, 490, 2948
Dietrich, T., Coughlin, M. W., Pang, P. T. H., et al. 2020, Sci, 370, 1450
Dietrich, T., & Hinderer, T. 2017, PhRvD, 95, 124006
East, W. E., Paschalidis, V., & Pretorius, F. 2016, CQGra, 33, 244004
Finn, L. S. 1992, PhRvD, 46, 5236
Graff, P. B., Buonanno, A., & Sathyaprakash, B. 2015, PhRvD, 92, 022002
Hild, S., Abernathy, M., Acernese, F., et al. 2010, CQGra, 28, 094013
Iyer, B., Souradeep, T., Unnikrishnan, C. S., et al. 2011, LIGO Document M1100296-v2, https://dcc.ligo.org/LIGO-M1100296/public
Khan, S., Husa, S., Hannam, M., et al. 2016, PhRvD, 93, 044007
Kyutoku, K., Ioka, K., Okawa, H., Shibata, M., & Taniguchi, K. 2015, PhRvD, 92, 044028
Lehner, L., Liebling, S. L., Palenzuela, C., & Motl, P. M. 2016, PhRvD, 94, 043003
Li, T. 2013, Extracting Physics from Gravitational Waves (Berlin: Springer)
LIGO Scientific Collaboration 2020, arXiv:2004.08342
London, L., Khan, S., Fauchon-Jones, E., et al. 2018, PhRvL, 120, 161102
Martynov, D., Miao, H., Yang, H., et al. 2019, PhRvD, 99, 102004
Messenger, C., & Read, J. 2012, PhRvL, 108, 091101
Nagar, A., Bernuzzi, S., Del Pozzo, W., et al. 2018, PhRvD, 98, 104052
Pan, Y., Buonanno, A., Boyle, M., et al. 2011, PhRvD, 84, 124052
Pan, Y., Buonanno, A., Taracchini, A., et al. 2014, PhRvD, D89, 084006
Pang, P. T. H., Calderón Bustillo, J., Wang, Y., & Li, T. G. F. 2018, arXiv:1802.03306
Pekowsky, L., Healy, J., Shoemaker, D., & Laguna, P. 2013, PhRvD, 87, 084008
Punturo, M., Abernathy, M., Acernese, F., et al. 2010a, CQGra, 27, 194002
Punturo, M., Abernathy, M., Acernese, F., et al. 2010b, CQGra, 27, 084007
Radice, D., Bernuzzi, S., & Ott, C. D. 2016, PhRvD, 94, 064011
Rao, R. 1992, Information and the Accuracy Attainable in the Estimation of Statistical Parameters (New York: Springer)
Reitze, D., Adhikari, R. X., Ballmer, S., et al. 2019, BAAS, 51, 35
Romano, J. D., & Cornish, N. J. 2017, LRR, 20, 2
Santamaria, L., Ohme, F., Ajith, P., et al. 2010, PhRvD, 82, 064016
Schutz, B. F. 1986, Natur, 323, 310
Smith, R. J. E., Ashton, G., Vajpeyi, A., & Talbot, C. 2020, MNRAS, 498, 4492
Taylor, S. R., & Gair, J. R. 2012, PhRvD, 86, 023502
Usman, S. A., Mills, J. C., & Fairhurst, S. 2019, ApJ, 877, 82
Varma, V., Ajith, P., Husa, S., et al. 2014, PhRvD, 90, 124004
Veitch, J., Del Pozzo, W., Williams, M., et al. 2020, johnveitch/cpnest: Release 0.10.2, Zenodo, doi:10.5281/zenodo.592884,
Wu, X.-P., Qin, B., & Fang, L.-Z. 1996, ApJ, 469, 48
Zimmerman, A., Haster, C.-J., & Chatziioannou, K. 2019, PhRvD, 99, 124044